

HOME > SCIENCE ADVANCES > VOL. 6, NO. 38 > HIGH-FREQUENCY MAGNETOACOUSTIC RESONANCE THROUGH STRAIN-SPIN COUPLING IN PERPENDICULAR MAGNETIC MULTILAYERS

RESEARCH ARTICLE APPLIED PHYSICS



High-frequency magnetoacoustic resonance through strain-spin coupling in perpendicular magnetic multilayers

DE-LIN ZHANG , JIE ZHU , [...], AND JIAN-PING WANG +4 authors [Authors Info & Affiliations](#)

SCIENCE ADVANCES 18 Sep 2020 Vol 6, Issue 38 DOI: 10.1126/sciadv.abb4607

2,257 13



Abstract

It is desirable to experimentally demonstrate an extremely high resonant frequency, assisted by strain-spin coupling, in **technologically important perpendicular magnetic materials for device applications**. Here, we directly observe the coupling of magnons and phonons in both time and frequency domains upon femtosecond laser excitation. This strain-spin coupling leads to a magnetoacoustic resonance in perpendicular magnetic [Co/Pd]_n multilayers, reaching frequencies in the extremely high frequency (EHF) band, e.g., 60 GHz. We propose a theoretical model to explain the physical mechanism underlying the strain-spin interaction. Our model explains the amplitude increase of the magnetoacoustic resonance state with time and quantitatively predicts the composition of the combined strain-spin state near the resonance. We also detail its precise dependence on the magnetostriction. The results of this work offer a potential pathway to manipulating both the magnitude and timing of EHF and strongly coupled magnon-phonon excitations.

METRICS & CITATIONS

SIGN UP FOR THE SCIENCEADVISER NEWSLETTER

The latest news, commentary, and research, free to your inbox daily

SIGN UP >

INTRODUCTION

The exploration of innovative approaches and new physics to couple energy transfer between magnons and phonons has recently renewed interest in both the scientific and technological communities (1, 2). Among the abundant physical phenomena (3–7) arising from the magnon-phonon coupling, the strain-assisted magnetoacoustic resonance in ferromagnetic (FM) materials provides an energetically efficient path for rapid switching of spin state, which is required for applications in cloud storage, advanced spin memory, logic, and other spintronic devices (8–10).

Strain can be launched by an ultrafast optical excitation, specifically femtosecond laser pulses, through thermal expansion (2, 11–15). The brief increase in thermal energy results in a local strain. This strain travels through the FM layers in the form of acoustic waves, with frequencies tunable by both the material composition and the layer geometry. In addition, the femtosecond laser pulses excite thermal demagnetization and thus introduce magnons (16). The acoustic waves act directly within the FM layer via magnetostriction (or the Villari effect) to couple with the magnetization. Thus, by simultaneously generating strain and spin within the FM layer, the ultrafast optical approach provides a powerful tool to initiate the coupling between phonons and magnons. The femtosecond time scale of the laser pulse is smaller than the relaxation time scales of phonons and magnons, which allows the capture of the magnon-phonon coupling processes in the time domain, such as strain-assisted large-angle magnetiza-

tion precession (2). In contrast, efforts have also been devoted to launching strain electrically by using piezoelectric materials (17–19), which induce a surface acoustic wave (SAW) in the substrate beneath the FM layer. In such experiments, the SAW propagates to the FM layer and modifies its FM properties by changing the lattice spacing, leading to a different phonon propagation direction.

Most experimental and theoretical studies of the magnon-phonon coupling in literature are focused on materials unsuitable for spintronic applications owing to their low resonant frequency or low Curie temperature, such as dilute magnetic semiconductor materials (20–24) and metallic FM materials [e.g., Terfenol-D (2), Gafenol (25, 26), Bi-YIG (27), and Ni (28–31)]. To date, direct experimental demonstration remains elusive for the magnon-phonon coupling, as well as ultrahigh frequency magnetoacoustic resonance in materials with perpendicular magnetic anisotropy (PMA). To remedy this, we choose [Co/Pd]_n multilayers as a model system in this work. These materials have high PMA at room temperature and a relatively large magnetostriction coefficient λ ($\sim 1 \times 10^{-4}$) (32, 33), holding great potential for various technological applications (34–38). Thus, they serve as an ideal platform for investigating the magnon-phonon coupling.

Here, we report an extremely high frequency (EHF) magnetoacoustic resonance up to 60 GHz in the PMA [Co/Pd]_n multilayer, originating from strong magnon-phonon coupling following excitation by femtosecond laser pulses. The resonance shows an enhanced wave envelope in the time domain, an anticrossing in the frequency domain, and substantial mixing of both magnons and phonons as predicted by a coupled model. These are also demonstrated by both ultrafast measurement signals and micromagnetic simulation. These observations all indicate that a hybridized quasiparticle composed of both magnon and phonon exists in perpendicular magnetic multilayers, whereby the energy transfers among magnon and phonon systems efficiently. This allows the acoustic wave to substantially influence the magnetization at an ultrafast picosecond scale. Thus, our work paves a potential pathway to enabling an EHF magnetoacoustic resonance through the magnon-phonon coupling and suggests a possibility of ultrahigh-speed strain-assisted magnetization switching in a technologically relevant magnetic system.

RESULTS

Sample characteristics and ultrafast instrumentation

Figure 1A illustrates the time-resolved magneto-optical Kerr effect (TR-MOKE) and time-domain thermoreflectance (TDTR) ultrafast measurement configurations, together with a schematic of the sample stack. The thermoreflectance signals collected in TDTR measurements are proportional to the intensity change in the reflectivity of the probe beam, which contain information of both temperature and acoustics (39, 40). Thus, the TDTR signals represent strain waves in the sample. The TR-MOKE method used here is a pump-probe technique capable of recording the time evolution of magnetization (**M**), through the change in the polarization of the probe beam reflected from FM films (39). Typically, raw signals from TR-MOKE measurements may contain non-MOKE components, whose contributions are found to be negligible in determining the frequencies and relaxation times of spin precession and acoustic waves. More details about the TDTR and TR-MOKE experiment techniques are provided in note S1.

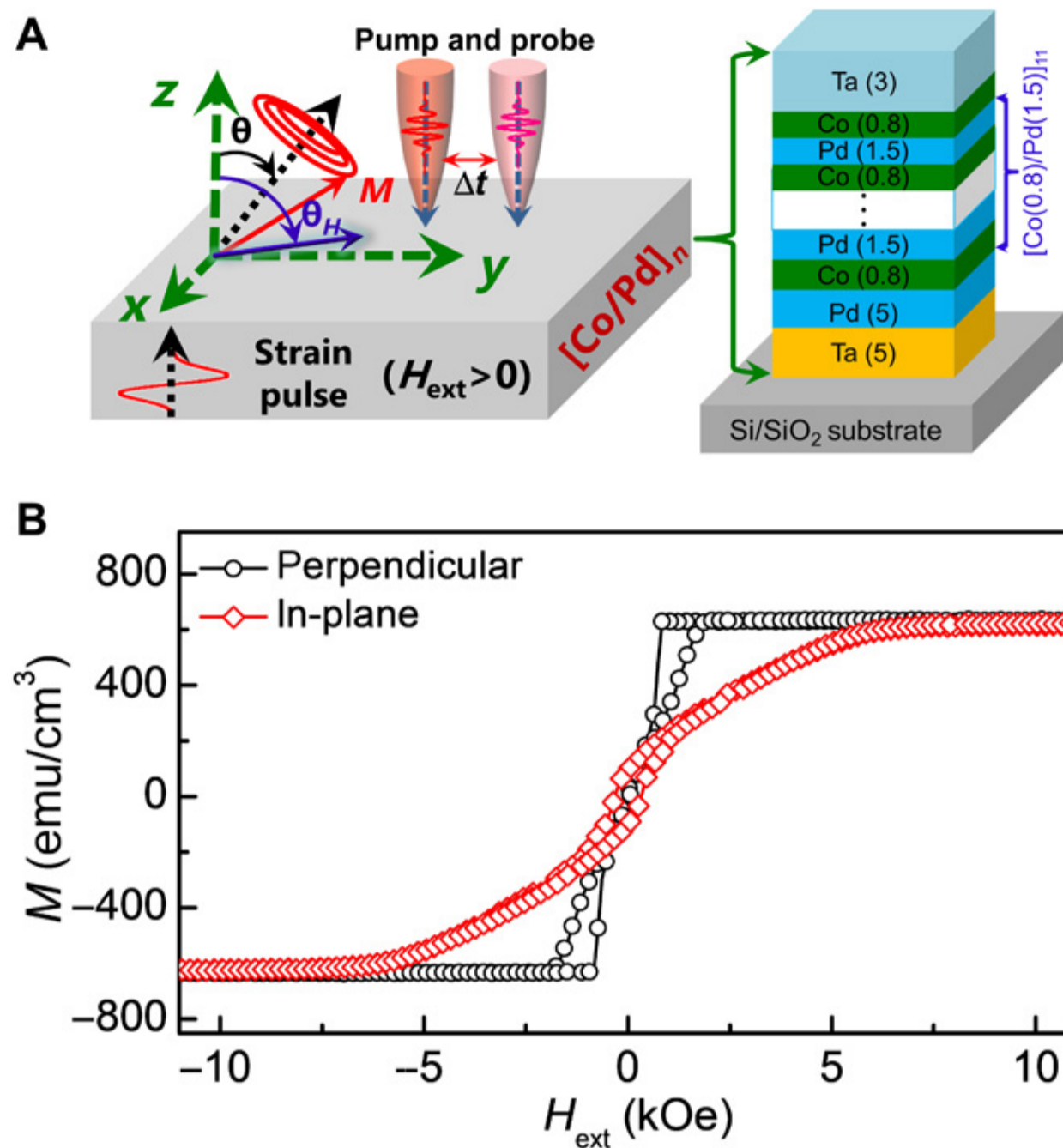


Fig. 1 Measurement protocol.

(A) Illustration of the ultrafast TR-MOKE measurements (left) on the $[\text{Co/Pd}]_n$ multilayer with numbers in parentheses denoting layer thicknesses in nanometers (right). In the TR-MOKE measurement, in the absence of an external magnetic field H_{ext} , the magnetostrictive effect can be measured, in which the acoustic strain wave induces the magnetization oscillation. The magnetization of the $[\text{Co/Pd}]_n$ multilayer is tilted to the angle (θ) when $H_{\text{ext}} > 0$ is applied with the angle $(\theta_H = 80^\circ)$. The TR-MOKE signals will include the signal from spin precession and acoustic strain wave. By fitting the data, we can separate them and identify their coupling. The figure in the right plane of the top shows the $[\text{Co/Pd}]_n$ multilayered structure used in our work. (B) The magnetic hysteresis (M - H) loops of the $[\text{Co}(0.8 \text{ nm})/\text{Pd}(1.5 \text{ nm})]_{11}$ multilayer with a magnetic anisotropy field $H_{k,\text{eff}}$ of ~ 6.5 kOe.

For a typical polar TR-MOKE measurement, a damped oscillation feature is expected in the signals due to the spin precession initiated by the rapid temperature rise from pump excitation, when an external magnetic field (H_{ext}) is applied (39). However, the TR-MOKE signals usually do not show magnetization oscillations in the absence of H_{ext} , since the equilibrium axis of the spin precession will be aligned with the surface normal direction of the perpendicular magnetic film. When the sample has a large magnetostriction constant λ , acoustic waves can tilt the magnetization and therefore create a detectable change in M_z and will be captured as magnetization oscillations in the signal as well. Thus, the magnetization oscillation features captured by TR-MOKE contains both the spin precession and acoustic wave information (20). Therefore, analyzing the data from both TDTR and TR-MOKE measurements allows for the investigation of the coupling between strain and spin. The TR-MOKE signals contain information of two behaviors, as the superposition of two frequencies in M_z : loosely categorized as the field-dependent one corresponding to the typical FM resonance (FMR) resulting from coherent spin precession and the field-independent one caused by a time-dependent modulation of magnetic properties through strain.

In our TR-MOKE signals for all the $[\text{Co/Pd}]_n$ samples, the magnetization oscillations appear without H_{ext} , implying that these samples have the magnetostriction effect, as discussed in note S1 and shown in figs. S3 and S4. By fitting the TR-MOKE data, we find that in relatively thin films, the strain frequency (>100 GHz) is much higher than that of spin precession (<60 GHz) with a relatively low H_{ext} , as shown in fig. S5. This frequency is for the lowest-frequency normal mode of the acoustic waves confined within the thin-film sample stack, whose half-wavelength depends on the thickness of the entire sample stack (including the capping and seed layers). Therefore, by changing the sample thickness, the strain frequency can be tuned (40). In this study, we select the $[\text{Co}(0.8 \text{ nm})/\text{Pd}(1.5 \text{ nm})]_{11}$ multilayered structure with a relatively large (25 nm) thickness as a model system. This $[\text{Co}(0.8 \text{ nm})/\text{Pd}(1.5 \text{ nm})]_{11}$ multilayer is seeded with a Ta(5 nm)/Pd(5 nm) bilayer deposited on a SiO_2 (300 nm)/Si substrate and is capped with a 3-nm Ta layer. It has perpendicular anisotropy with an effective field of $H_{k,\text{eff}} \sim 6.5$ kOe and magnetic anisotropy of $K_u \sim 4.4 \times 10^6$ erg/cm³, as shown in Fig. 1B.

Ultrafast measurement results

The TR-MOKE results of [Co(0.8 nm)/Pd(1.5 nm)]₁₁ with the range of H_{ext} from 10 to 29 kOe are plotted in Fig. 2A. We find that for $18 \text{ kOe} < H_{\text{ext}} < 24 \text{ kOe}$, TR-MOKE signals show that the amplitude of precessional oscillations of M_z increases instead of the usual decrease in the first 60 ps following the pump excitation. However, when H_{ext} is smaller than 18 kOe or larger than 24 kOe, the TR-MOKE signals in Fig. 2A appear as the typical monotonic decaying trend of damped oscillations (standard in TR-MOKE measurements of magnetization precession). Within the first several picoseconds, different energy carriers such as magnons, phonons, and electrons induced by the ultrafast laser pulse are out of equilibrium with each other. As the main goal of this work is to analyze the magnetic precession that is in the equilibrium regime, we purposefully start the fitting from 10 ps to avoid any possible nonequilibrium effect (indicated by the solid lines in Fig. 2A). From Fig. 2B of TDTR data, we can find that the acoustic strains prevail in the first 60 ps. For the range of $18 \text{ kOe} < H_{\text{ext}} < 24 \text{ kOe}$, the injected energy by the strain overcomes the magnetically dissipated energy, leading to the enhanced amplitude of spin precession roughly within this first 60 ps, in contrast to the monotonic decaying trend of a typical damped feature of spin precession at other fields. After 60 ps, the injected energy by the strain is insufficient to compensate for the dissipated energy due to the damping and, thus, is not capable of maintaining the high-energy state (the magnetoacoustic resonance state as explained later). The spin oscillation amplitude decreases, and the typical damped feature appears.

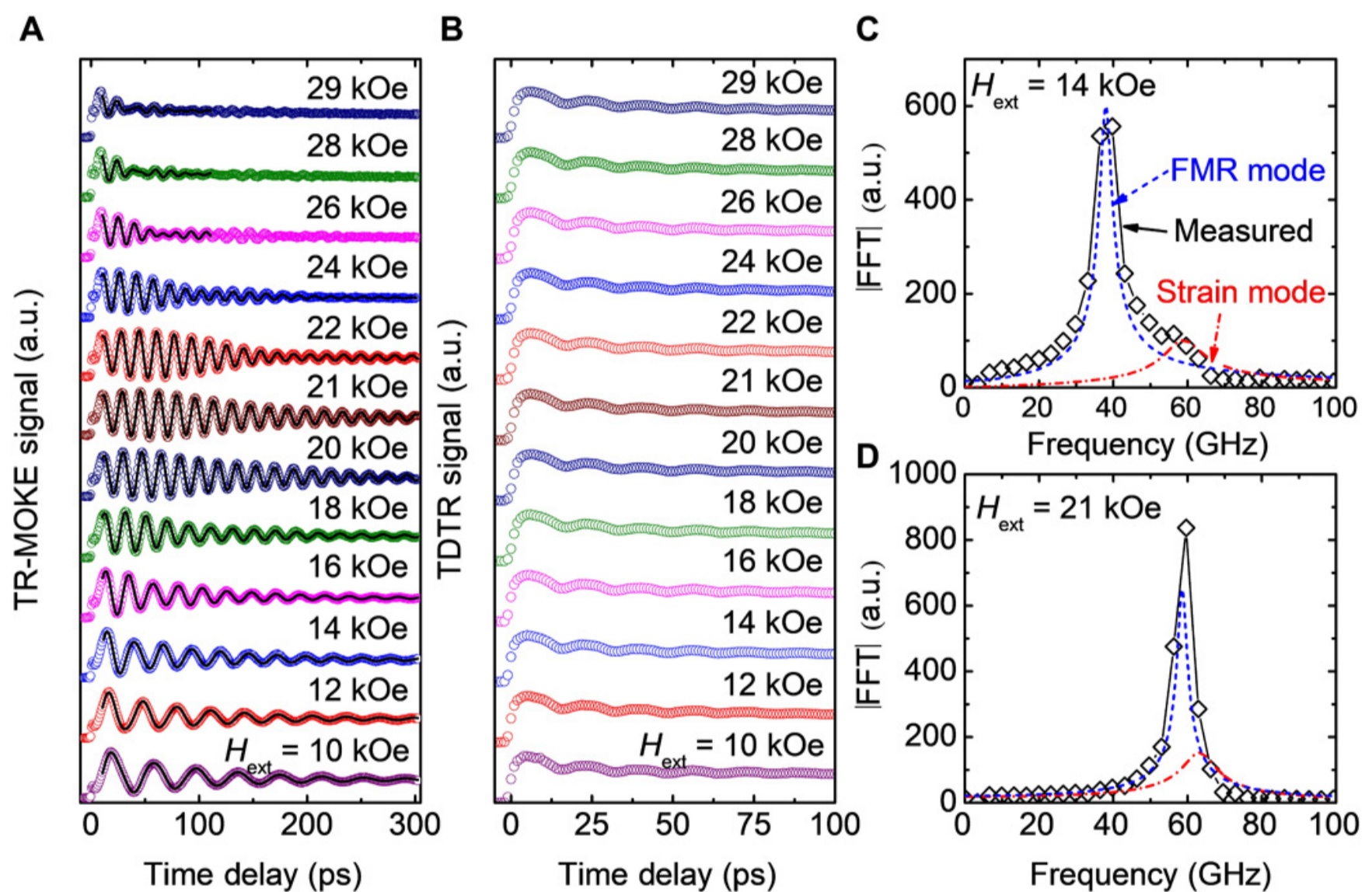


Fig. 2 Ultrafast measurement results.

(A) The experimental and fitted TR-MOKE signals and (B) the experimental TDTR signals as a function of H_{ext} (10 to 29 kOe). It is clearly seen that TDTR signals do not change in the whole region of H_{ext} , while TR-MOKE signals show different oscillation patterns with external fields. For $H_{\text{ext}} < 18 \text{ kOe}$ or $H_{\text{ext}} > 24 \text{ kOe}$, magnetization precession presents a damped oscillation, while for $18 \text{ kOe} < H_{\text{ext}} < 24 \text{ kOe}$, it shows a resonance phenomenon. (C and D) Fourier transform of the TR-MOKE signals with $H_{\text{ext}} = 14 \text{ kOe}$ and 21 kOe , respectively, from which two peaks (FMR and strain) can be found. For $H_{\text{ext}} = 14 \text{ kOe}$, the two peaks are separate; however, the two peaks are overlapping when $H_{\text{ext}} = 21 \text{ kOe}$. a.u., arbitrary units.

To further understand the magnetization dynamics and magnetoacoustic resonance resulting from the coupling between strain and spin, the TR-MOKE and TDTR signals of the [Co(0.8 nm)/Pd(1.5 nm)]₁₁ sample are analyzed in the time domain using the following equation

$$V(t) = A + Be^{-t/C} + D_1 \sin(2\pi f_1 t + \varphi_1) e^{-t/\tau_1} + D_2 \sin(2\pi f_2 t + \varphi_2) e^{-t/\tau_2} \quad (1)$$

where V is the signal; t is the time; A , B , and C are fitting parameters of the thermal background; D_i represents the amplitude of sinusoid; f_i is the frequency; φ_i is the phase; and τ_i is the relaxation time. The indices of $i = 1, 2$ represent two separate modes (low-frequency mode 1 and high-frequency mode 2 as defined later), captured by the measurement simultaneously (41, 42). The TDTR data only show one frequency corresponding to the picosecond

acoustics (strain) in the system, which is independent of the external field. Fitting the TR-MOKE data (which captures the change in the z component of magnetization) shows two distinct frequencies over most of the range: a frequency that depends on H_{ext} following a Kittel dispersion (FMR) and a frequency that is independent of H_{ext} that matching the frequency of the strain captured by TDTR (strain). More details about the amplitude and phase information of these two behaviors are provided in note S1. Two TR-MOKE signals, one in resonance ($H_{\text{ext}} = 21$ kOe) and the other one out of magnetoacoustic resonance ($H_{\text{ext}} = 14$ kOe), are chosen for comparison to study the coupling between spin precession and acoustic waves (Fig. 2C). We find that the frequency of the signal without the magnetoacoustic resonance shows two distinct peaks that are well separated, ~ 38 GHz for spin precession and ~ 60 GHz for the acoustic waves. However, for the signal at the magnetoacoustic resonance, two frequency peaks are overlapping at ~ 60 GHz, as plotted in Fig. 2D. This suggests that the magnetoacoustic resonance originates from the strong coupling between strain and spin.

Extremely high-frequency magnetoacoustic resonance

Figure 3 (A and C) plots the frequencies of spin precession of the $[\text{Co}(0.8 \text{ nm})/\text{Pd}(1.5 \text{ nm})]_{11}$ multilayer, which are fitted from the TR-MOKE signal as a function of H_{ext} based on Eq. 1. There are two modes, the low-frequency mode being labeled mode 1 (open black circles) and the high-frequency mode being labeled mode 2 (open red diamonds). These two modes are weakly coupled; i.e., the coupling is small compared to the frequency difference, except near the resonance with a coupling coefficient κ of $\sim (16.5 \text{ GHz})^2 = 272 \text{ GHz}^2$ that is determined by the magnetostriction coefficient, magnetic properties, and the external field angle (details in note S3D). At low fields where ω_1 is much smaller than ω_2 , these modes are distinctly separated by the driving mechanism. The largest TR-MOKE signal corresponds to the low-frequency mode, driven directly by magnon from the fast demagnetization process. The frequency of mode 1 (ω_1) is equal to the magnon frequency ω_M and is linearly dependent on H_{ext} , with a slope of $\gamma/2\pi$ with γ being the gyromagnetic ratio. The displacement of this linear behavior of ω_1 is caused by the effective anisotropy field. The amplitude m_0 depends on the initial precession angle (the maximum value of $\sim 1^\circ$), estimated based on the conversion from TR-MOKE voltage to the Kerr angle. m_0 decreases rapidly when increasing external magnetic field as $1/H_{\text{ext}}^2$, due to the energy gradient change according to the “law of approach to saturation” (43). The high-frequency mode 2 is weakly detected because it is primarily phonon-based. Its frequency ω_2 is field independent at low fields, remaining at a constant 60 GHz, with the phonon frequency ω_{ph} fitted from TDTR signals (blue stars). Its amplitude $\kappa\eta_0/(\omega_{\text{ph}}^2 - \omega_M^2)$ is proportional to the strain amplitude η_0 and the coupling coefficient κ (note S3D). This indicates that the high-frequency mode ω_2 makes a negligible contribution to the magnon-dominated dynamics at low fields, verified by a slight side peak appearing in the FFT spectrum in Fig. 2C. The amplitude gradually increases when increasing the magnetic field, as the difference between ω_M and ω_{ph} shrinks.

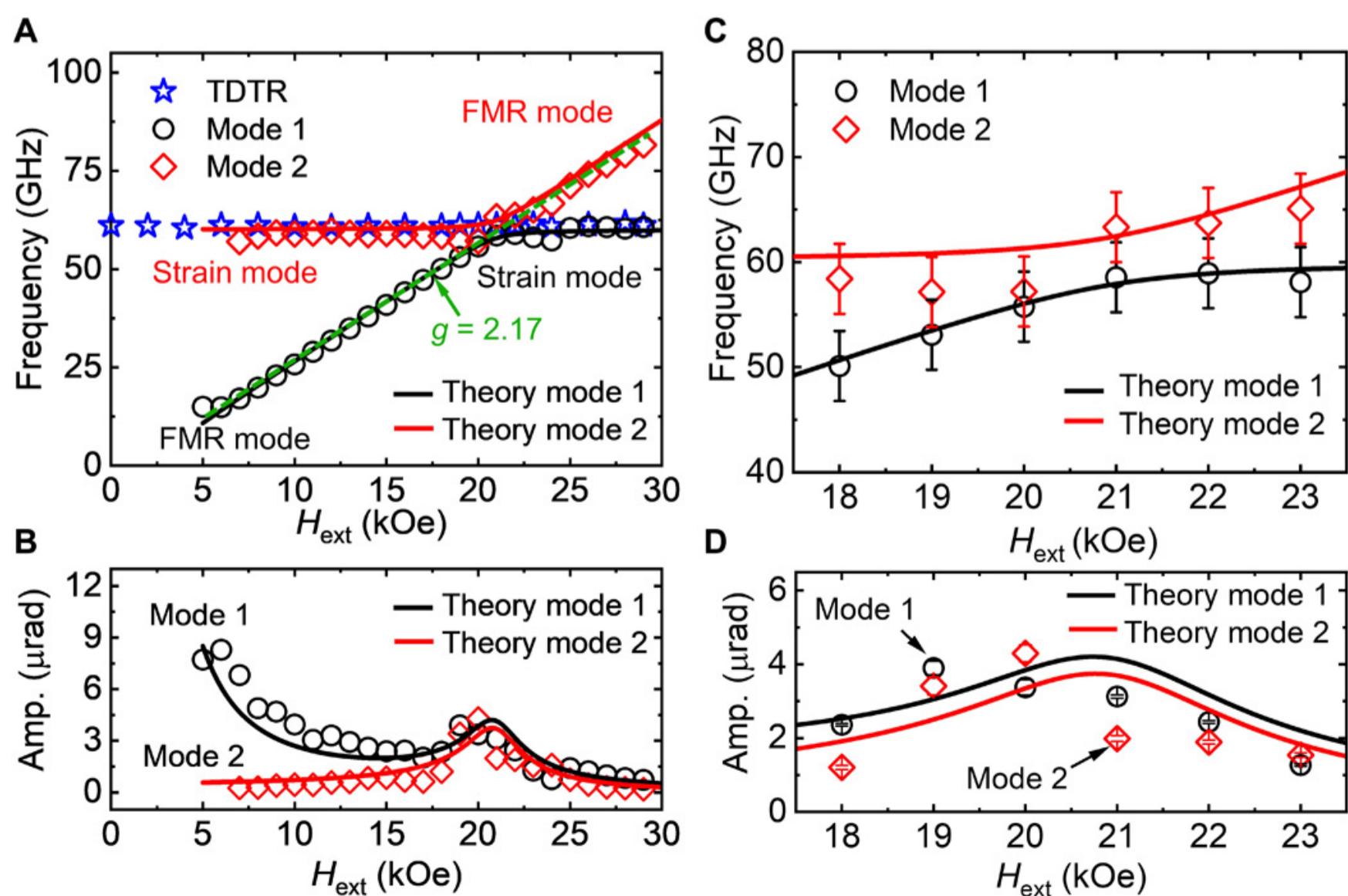



Fig. 3 High-frequency magnetoacoustic resonance.

(A) The frequency of the $[\text{Co}(0.8 \text{ nm})/\text{Pd}(1.5 \text{ nm})]_{11}$ multilayer as a function of H_{ext} . Two frequencies of spin precession (mode 1, open black circles; mode 2, open red diamonds) are derived by fitting the experimental data of TR-MOKE. The figure also includes the frequency of acous-

tic waves measured from TDTR (blue stars). The anticrossing point of mode 1 and mode 2 occurs at the resonance field ($H_{\text{ext}} \approx 21$ kOe), where

Expand for more 

When the frequencies of these two modes approach each other, the high- and low-frequency modes hybridize, reflecting strongly coupled magnon-phonon dynamics. The two modes, driven by a quasiparticle with substantial contributions from both magnon and phonon, deviate from their original characteristics discussed in the previous low-field condition. The frequencies of modes 1 and 2 display an anticrossing with a frequency gap Δf , deviating from the original $\omega_M (\approx \omega_1)$ or $\omega_{\text{ph}} (\approx \omega_2)$. The nature or presence of an anticrossing feature cannot be proven to high confidence due to the experimental error bars, so our real evidence for anticrossing comes from theory. Clearly, the strain drives the magnetization oscillations, which can only happen if they have the same symmetry. Therefore, there must be a mixing term in the Hamiltonian, and an anticrossing is guaranteed. To quantitatively predict the gap Δf , we calculate the two frequencies of modes 1 and 2 at the resonance point (defined as $\omega_M = \omega_{\text{ph}}$ at $H_{\text{ext}} \approx 21$ kOe), which gives $\omega_1 = \omega_{\text{ph}} - (\kappa/2\omega_{\text{ph}})$ and $\omega_2 = \omega_{\text{ph}} + (\kappa/2\omega_{\text{ph}})$. This yields $\Delta f = \omega_2 - \omega_1 = 4.6$ GHz, which is consistent with experimental data using no fitting parameters, as shown in [Fig. 3 \(A and C\)](#). The hybridization regime is defined as H_{ext} at which $|\omega_M - \omega_{\text{ph}}|$ approximates $\kappa/\omega_{\text{ph}}$, leading to a range of 19.7 kOe $< H_{\text{ext}} < 22.1$ kOe. The amplitudes of both modes increase in the hybridization regime, as shown in [Fig. 3 \(B and D\)](#). The original phonon-driven mode is now highly visible owing to the admixed magnon, where its amplitude changes from a negligible value ($\sim \eta_0$) to a notable value. The original magnon-driven mode is enhanced owing to the pumping from phonon, where its amplitude enhancement is caused by the strain amplitude η_0 , which also results in magnon-phonon hybridization. In addition, this hybridization appears as a magnetoacoustic resonance at the resonance field (the strongest effect) and nearby, as verified by the enhanced wave envelope in the TR-MOKE signals in [Fig. 2A](#). We can conclude that the magnon-phonon coupling substantially influences the spin dynamics and induces a resonant state. When further increasing H_{ext} from the resonance-field range, the frequencies of these two modes move apart again. At such high fields, the hybridization disappears, and the modes are distinctly driven by the phonon or magnon. The low-frequency mode 1 becomes the phonon-driven mode ($\omega_1 \approx \omega_{\text{ph}}$), while the high-frequency mode 2 is the magnon-driven mode $\omega_2 = \omega_M$. Their behaviors are very similar to those at low fields.

DISCUSSION

To accurately describe the time-domain behavior and compare directly with TR-MOKE signals, we use micromagnetic simulations based on the Landau-Lifshitz-Gilbert equation, including the magnetostriction effect and the damping. The simulation reproduces the resonant state, whereby the wave envelope rises for ~ 100 ps and afterward follows a standard relaxation, as shown in [Fig. 4B](#). Comparing with the experimental data from TR-MOKE ([Fig. 4A](#)), the theoretical model we propose here can capture all the key features in this ultrafast magnon-phonon coupling behavior. From the energy perspective, the phonon initially pumps enough energy into the magnon system to overwhelm the energy dissipation (fig. S6). This energy enhancement excites the magnetization to precess in a larger angle, presenting a rise, rather than the immediate decay found for the off-resonance condition, as observed in [Fig. 2A](#) for the low- and high-field cases. The simulation uses the same material magnetostriction coefficient (details in note S3) and thus the same coupling coefficient as used in the previous section to predict the frequencies of modes 1 and 2. The rising time depends on the coupling coefficient κ . Relaxation occurs when the pumped energy by phonon is no longer sufficient to compensate for the dissipated energy. The overall agreement of experiment and theory suggests that our assumption of a uniform spin mode is correct, although the existence of the lowest exchange magnon cannot be completely excluded ([29](#)).

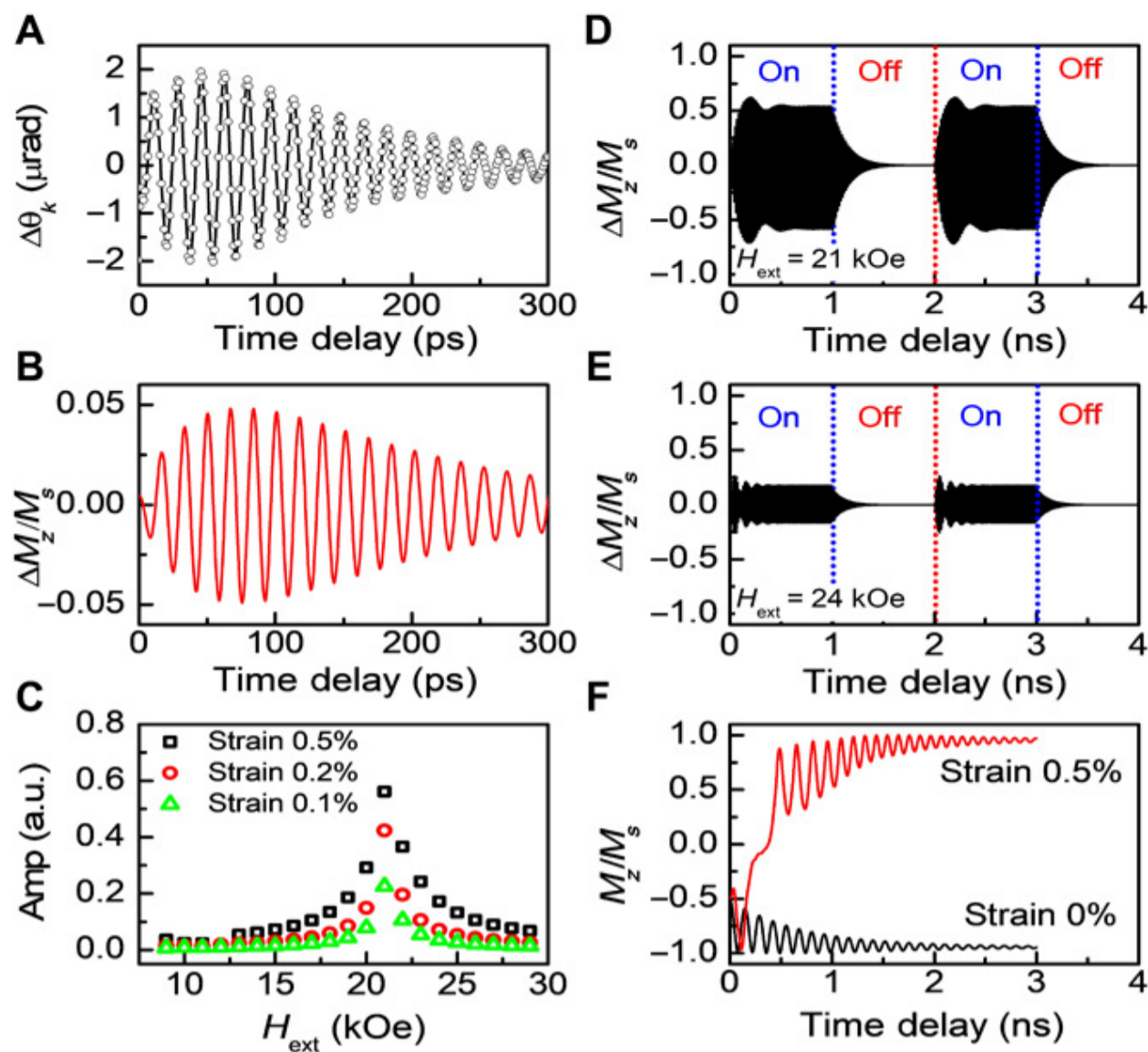


Fig. 4 Time-dependent magnetization dynamics.

(A and B) The experimental and simulated TR-MOKE signal of the $[\text{Co}(0.8 \text{ nm})/\text{Pd}(1.5 \text{ nm})]_{11}$ multilayer with $H_{\text{ext}} = 21 \text{ kOe}$, respectively. The strain used to produce the simulated signal is 0.5%. (C) The oscillation amplitude versus H_{ext} for different strain amplitudes (0.1, 0.2, and 0.5%). (D and E) The time evolution of the out-of-plane magnetization (M_z) versus the time delay when a square strain pulse is applied. The pulse amplitude is 0.5%, the time period is 2.0 ns, and the pulse length is 1.0 ns. The simulated spin precession coupled with a 0.5% strain pulse under an H_{ext} of 21 kOe (D) and 24 kOe (E), respectively. When the strain pulse is on, the system gets excited rapidly to an enhanced large-angle precession with a rise time of $\sim 100 \text{ ps}$ under $H_{\text{ext}} = 21 \text{ kOe}$, but not 24 kOe. When the strain pulse is off, the system at these H_{ext} values shows relaxation behavior. (F) Strain-assisted switching for $[\text{Co}(0.8 \text{ nm})/\text{Pd}(1.5 \text{ nm})]_{11}$ with $H_{\text{ext}} = 1 \text{ kOe}$. When strain is absent in the system (strain amplitude of 0%), switching does not occur (shown by the black line). When strain (strain amplitude of 0.5%) is applied, switching occurs (shown by the red line).

Time-dependent magnetization dynamics driven by acoustic waves

To prove that acoustic waves can manipulate the magnetization and further assist the switching on an ultrafast picosecond scale, we carried out the micromagnetic simulation of the out-of-plane magnetization (M_z) versus the time delay with a square strain pulse. The strain pulse amplitude is 0.5%, the pulse period is 2 ns, and the pulse length is 1 ns. [Figure 4 \(D and E\)](#) shows M_z versus time delay of the system at two external fields near the magnetoacoustic resonance state. When the strain pulse is on, the system becomes excited rapidly to an enhanced large-angle precession with a rise time of $\sim 100 \text{ ps}$. When the strain pulse is off, the system at both external magnetic fields shows relaxation behavior, and the magnetization becomes aligned with H_{ext} . This large-angle precession caused by the resonance between acoustic waves and spin precession is maintained steadily for nondecaying strain amplitude. In addition, as the spin dynamics is a nonlinear system, the resonance can happen in a wide field range of several kOe, centered at the resonance point with a field range determined by the coupling coefficient κ ([Fig. 4C](#)). For example, an external magnetic field of $H_{\text{ext}} = 21 \text{ kOe}$ has the maximum precession amplitude, while fields of $H_{\text{ext}} = 18 \text{ kOe}$ or 24 kOe can also excite resonant behavior with relatively smaller precession amplitudes. It can also be seen that the precession amplitudes with 0.2 or 0.5% strain yield similar peak values. The magnetoacoustic resonance with $H_{\text{ext}} = 21 \text{ kOe}$ is enhanced when the strain increases from 0.1 to 0.2% (see [fig. S7](#)). This level of strain has been detected by previous researchers ([44, 45](#)). [Figure 4F](#) presents the strain-assisted magnetization switching of the $[\text{Co}(0.8 \text{ nm})/\text{Pd}(1.5 \text{ nm})]_{11}$ system with $H_{\text{ext}} = 1 \text{ kOe}$. It is clearly seen that when strain is absent in the system (strain amplitude of 0%), the magnetization of the system shows the normal damped decay and switching does not happen. When strain (strain amplitude of 0.5%) is applied, the system shows a large-angle magnetization precession and switching occurs in 3 ns. We also note that [Vlasov et al. \(46\)](#) have recently predicted switching in an elliptical nanomagnet with shape anisotropy.

CONCLUSION

We experimentally detect acoustic waves with response time down to the order of 10 ps in perpendicular magnetic $[\text{Co}/\text{Pd}]_n$ multilayers via a femtosecond laser pulse excitation. Through direct measurements of coherent phonons and magnetization, we observe a 60-GHz magnetoacoustic resonance when the frequencies of acoustic waves and

spin precession approach each other. We develop a theoretical model and revealed the physical mechanism of magnetoacoustic resonance from the strain-spin interaction within an energy viewpoint. This model and experiment agree in their demonstration of hybridization between strain and spin waves near the resonance point. The results, by illustrating a pathway to switching the magnetization of a high anisotropy perpendicular material through strain-spin coupling, offer an approach to meeting the future technological needs of high speed and highly compact memory.

MATERIALS AND METHODS

Sample preparation and characterization

All samples with the stack of $[\text{Co}(x)/\text{Pd}(y)]_n/\text{Co}(x)/\text{Ta}(3)$ ($x = 0.30$ to 0.70 nm; $y = 0.70$ to 1.80 nm), from the bottom to top, are deposited on Si/SiO_2 (300 nm) substrate at room temperature using a six-target Shamrock magnetron sputtering system with the ultrahigh vacuum (base pressure $< 5.0 \times 10^{-8}$ torr). The $[\text{Co}(0.8 \text{ nm})/\text{Pd}(1.8 \text{ nm})]_{11}$ multilayer is seeded with the $\text{Ta}(5 \text{ nm})/\text{Pd}(5 \text{ nm})$ bilayer; the others are seeded with the $\text{Ta}(3 \text{ nm})/\text{Pd}(3 \text{ nm})$ bilayer. All layers are sputtered with dc power sources and element targets under an Ar working pressure of 2.0 mtorr. The magnetic properties of all samples are characterized using a Physical Property Measurement System with the Vibrating Sample Magnetometer module.

TR-MOKE and TDTR measurements

Both TDTR and TR-MOKE methods are based on the ultrafast pump-probe technique. In this technique, pump pulses are used to excite the sample to a higher energy level followed by a recovery process, while probe pulses detect this change as a function of time delay. A mode-locked Ti:Sapphire laser with a pulse duration of ~ 100 fs and a center wavelength of 783 nm at a repetition rate of 80 MHz is used for TDTR and TR-MOKE measurements. A $10\times$ objective lens is used to produce a $1/e^2$ spot radius of $w_0 = 6 \mu\text{m}$ for both pump and probe beams. In addition, an external magnetic field of up to 29 kOe (at $\theta_H = 80^\circ$ as defined in Fig. 1A) is applied in both TR-MOKE and TDTR measurements. The TDTR signal is captured with a fast-response photodiode, while the TR-MOKE signal is captured with a balanced detector. For our measurement setup, the field angle is limited to $80^\circ \leq \theta_H \leq 90^\circ$ to achieve sufficiently high fields and to ensure a clear optical path for the laser beam. Therefore, we set θ_H to be 80° for all measurements of $[\text{Co}/\text{Pd}]_n$ samples, to achieve the highest precessional frequency with the smallest field and, meanwhile, to maximize the TR-MOKE signals (see note S1).

Theory model and micromagnetic simulation

In the theoretical model, we first derive the magnetic dynamics, in Eq. 2 under the influence of the magnetostriction and the damping effect, from the macrospin model. Unlike (30, 31), the role of backaction is included, which allows predictions for the experimentally observed hybridization. We define that the z' axis is tilted from the original z axis with an angle θ'_H ($\theta'_H = \pi/2 - \theta_H$) and perpendicular to the original x axis. The equation for the out-of-plane magnetization $m_{z'}$ is

$$\frac{d^2 m_{z'}}{dt^2} + \omega_M^2 m_{z'} + \Gamma \frac{dm_{z'}}{dt} = -\kappa\eta \quad (2)$$

where ω_M is the magnetic frequency, Γ is the relaxation rate, and κ is the coupling coefficient. The explicit expressions for these parameters are

$$\omega_M = \gamma \sqrt{(H_{\text{ext}} + H_{k0} \sin \theta'_H)(H_{\text{ext}} - H_{k0} \cos(2 \theta'_H))} \quad (3)$$

$$\Gamma = \alpha \gamma (2 H_{\text{ext}} + H_{k0} \sin^2 \theta'_H - H_{k0} \cos(2 \theta'_H)) \quad (4)$$

$$\kappa = 3\gamma^2 / 8 (H_{\text{ext}} + 2 H_{k0} \sin^2 \theta'_H) \sin(2 \theta'_H) (b_2 / M_s) \quad (5)$$

where γ is gyromagnetic ratio, H_{ext} is external bias field, H_{k0} is the effective perpendicular anisotropy, and b_2 is the magnetostriction coefficient. Details may be found in note S3A.

The strain amplitude η is governed by

$$\frac{d^2\eta}{dt^2} + \omega_{\text{ph}}^2\eta = -\kappa m_z' \quad (6)$$

where ω_{ph} is the phonon frequency. [Equations 2](#) and [6](#) yield the characteristics of the two modes in the magnetic dynamics, as low-frequency mode ω_1 and high-frequency mode ω_2 . Their amplitudes are B_1 and B_2 , correspondingly. Approximations under varying conditions are performed in note S3D to aid physical understanding and are summarized in Discussion.

$$\omega_1 = \sqrt{\left(\omega_M^2 + \omega_{\text{ph}}^2 - \sqrt{(\omega_M^2 - \omega_{\text{ph}}^2)^2 + 4\kappa^2}\right)/2} \quad (7)$$

$$\omega_2 = \sqrt{\left(\omega_M^2 + \omega_{\text{ph}}^2 + \sqrt{(\omega_M^2 - \omega_{\text{ph}}^2)^2 + 4\kappa^2}\right)/2} \quad (8)$$

$$B_1 = \frac{m_0 + \eta_0 \frac{\kappa}{\omega_M^2 - \omega_2^2}}{1 - \frac{\kappa}{\omega_M^2 - \omega_2^2} \frac{\kappa}{\omega_{\text{ph}}^2 - \omega_1^2}} \quad (9)$$

$$B_2 = \frac{-\frac{\kappa}{\omega_M^2 - \omega_2^2} \eta_0 - m_0 \frac{\kappa}{\omega_{\text{ph}}^2 - \omega_1^2} \frac{\kappa}{\omega_M^2 - \omega_2^2}}{1 - \frac{\kappa}{\omega_M^2 - \omega_2^2} \frac{\kappa}{\omega_{\text{ph}}^2 - \omega_1^2}} \quad (10)$$

where m_0 is the initial magnetization out-of-plane component m_0 deviating from the final equilibrium position. η_0 is the initial strain amplitude.

Third, we perform micromagnetic simulation to accurately describe the magnetic dynamics versus time, including both the magnetostrictive and damping effect. We choose the experimental initial conditions in the simulation. Through a straightforward voltage to Kerr angle conversion in TR-MOKE signal, a precessional cone angle (maximum value of $\sim 1^\circ$) is used to set the initial magnetization condition in simulation (see note S2). A strain of 0.1% is used to set the initial strain condition.

Acknowledgments

We thank P. Crowell from University of Minnesota for valuable discussions and suggestions. **Funding:** This work was partially supported by C-SPIN, one of six centers of STARnet, a Semiconductor Research Corporation program, sponsored by MARCO and DARPA, and by ASCENT, one of six centres in JUMP, a Semiconductor Research Corporation program, sponsored by MARCO and DARPA. D.M.L. and X.W. thank the support from Advanced Storage Research Consortium (ASRC). The authors acknowledge the Minnesota Supercomputing Institute (MSI) at the University of Minnesota for providing resources that contributed to the research results reported within this paper. Revisions to this paper have been funded by the Center for Micromagnetics and Information Technologies (MINT). **Author contributions:** D.-L.Z., J.Z., T.Q., R.H.V., X.W., and J.-P.W. conceived the research. D.-L.Z. designed and prepared all of the samples and carried out all magnetic measurements. J.Z. and D.M.L. designed and carried out the TDTR and TR-MOKE measurements and fitted the data. D.-L.Z. and J.Z. introduced the initial experimental results including magnetic properties and TDTR and TR-MOKE data on this topic to T.Q. and suggested the need for theoretical analysis. T.Q. carried out the theoretical prediction, analytical derivation, and micromagnetic simulation that inspired the experimental results of the resonance. D.-L.Z. and J.Z. participated in the discussion of the theory and micromagnetic simulation. D.-L.Z., J.Z., and T.Q. prepared the figures and drafted the manuscript. J.-P.W., X.W., and R.H.V. coordinated the project. All the authors discussed the results and commented on the manu-

script. **Competing interests:** The authors declare that they have no competing interests. **Data and materials availability:** All data needed to evaluate the conclusions in the paper are present in the paper and/or the Supplementary Materials. Additional data related to this paper may be requested from the authors.

Supplementary Material

File (abb4607_sm.pdf)

DOWNLOAD

1.16 MB

REFERENCES AND NOTES

- 1 A. Kirilyuk, A. V. Kimel, T. Rasing, Ultrafast optical manipulation of magnetic order. *Rev. Mod. Phys.* **82**, 2731–2784 (2010).
[↶ GO TO REFERENCE](#) • [CROSSREF](#) • [ISI](#) • [GOOGLE SCHOLAR](#)
- 2 O. Kovalenko, T. Pezeril, V. V. Temnov, New concept for magnetization switching by ultrafast acoustic pulses. *Phys. Rev. Lett.* **110**, 266602 (2013).
[+ SEE ALL REFERENCES](#) • [CROSSREF](#) • [PUBMED](#) • [ISI](#) • [GOOGLE SCHOLAR](#)

SHOW ALL REFERENCES

eLetters (0)

eLetters is a forum for ongoing peer review. eLetters are not edited, proofread, or indexed, but they are screened. eLetters should provide substantive and scholarly commentary on the article. Embedded figures cannot be submitted, and we discourage the use of figures within eLetters in general. If a figure is essential, please include a link to the figure within the text of the eLetter. Please read our [Terms of Service](#) before submitting an eLetter.

LOG IN TO SUBMIT A RESPONSE

No eLetters have been published for this article yet.

CURRENT ISSUE



The magmatic system under Hunga volcano before and after the 15 January 2022 eruption

BY HÉLÈNE LE MÉVEL, CRAIG A. MILLER, *ET AL.*

Driving forces of Antarctic krill abundance

BY ALEXEY RYABOV, UTA BERGER, *ET AL.*

Aqueous breakdown of aspartate and glutamate to n- ω -amino acids on the parent bodies of carbonaceous chondrites and asteroid Ryugu

BY YAMEI LI, HIROYUKI KUROKAWA, *ET AL.*

[TABLE OF CONTENTS >](#)

Sign up for ScienceAdviser

Subscribe to *ScienceAdviser* to get the latest news, commentary, and research, free to your inbox daily.

[SUBSCRIBE >](#)

LATEST NEWS

NEWS | 19 DEC 2023

[Why do most dogs have brown eyes?](#)

NEWS | 18 DEC 2023

[This algorithm could predict your health, income, and chance of premature death](#)

NEWS | 18 DEC 2023

[Chimps remember the faces of old friends and family for decades](#)

NEWS | 18 DEC 2023

[Vocal therapy changes vocal cords of transgender patients without need for surgery](#)

SCIENCEINSIDER | 18 DEC 2023

[Disgraced surgeon Paolo Macchiarini, whose crimes inspired an opera, headed to prison](#)

SCIENCEINSIDER | 15 DEC 2023

[NIH advisory group recommends \\$14,000 boost in postdoc pay](#)

RECOMMENDED

REPORTS | JULY 2006

[Low-Frequency Spin Dynamics in a Canted Antiferromagnet](#)

RESEARCH ARTICLE | JULY 2020

[Accessing new magnetic regimes by tuning the ligand spin-orbit coupling in van der Waals magnets](#)

RESEARCH ARTICLE | JANUARY 2018

[Observation of spin-orbit magnetoresistance in metallic thin films on magnetic insulators](#)

RESEARCH ARTICLE | OCTOBER 2020

[Electric-field control of spin dynamics during magnetic phase transitions](#)

[View full text](#) | [Download PDF](#)

Science

Science
Advances

Science
Immunology

Science
Robotics

Science
Signaling

Science
Trans
Med

FOLLOW US



GET OUR NEWSLETTER

NEWS

[All News](#)

[ScienceInsider](#)

[News Features](#)

[Subscribe to News from Science](#)

[News from Science FAQ](#)

[About News from Science](#)

CAREERS

[Careers Articles](#)

[Find Jobs](#)

[Employer Hubs](#)

COMMENTARY

JOURNALS

[Opinion](#)

[Analysis](#)

[Blogs](#)

[Science](#)

[Science Advances](#)

[Science Immunology](#)

[Science Robotics](#)

[Science Signaling](#)

[Science Translational Medicine](#)

[Science Partner Journals](#)

AUTHORS & REVIEWERS

[Information for Authors](#)

[Information for Reviewers](#)

LIBRARIANS

[Manage Your Institutional Subscription](#)

[Library Admin Portal](#)

[Request a Quote](#)

[Librarian FAQs](#)

ADVERTISERS

[Advertising Kits](#)

[Custom Publishing Info](#)

[Post a Job](#)

RELATED SITES

[AAAS.org](#)

[AAAS Communities](#)

[EurekAlert!](#)

[Science in the Classroom](#)

ABOUT US

[Leadership](#)

[Work at AAAS](#)

[Prizes and Awards](#)

HELP

[FAQs](#)

[Access and Subscriptions](#)

[Order a Single Issue](#)

[Reprints and Permissions](#)

[TOC Alerts and RSS Feeds](#)

[Contact Us](#)